Bioconjugate Chemistry

Article

pubs.acs.org/bc

Superparamagnetic Nanoparticles as High Efficiency Magnetic Resonance Imaging T_2 Contrast Agent

Fernanda Sousa,[†,‡,○] Barbara Sanavio,[*,†,○] Alessandra Saccani,[†] Yun Tang,[§,∥] Ileana Zucca,[⊥] Tamara M. Carney,[§] Alfonso Mastropietro,[⊥] Paulo H. Jacob Silva,[§] Randy P. Carney,[§] Kurt Schenk,[#] Arash O. Omrani,[▽] Ping Huang,[▽] Lin Yang,[▽] Henrik M. Rønnow,[▽] Francesco Stellacci,[*,§] and Silke Krol[†]

[†]Nanomedicine Laboratory, Fondazione IRCCS Istituto Neurologico Carlo Besta, AMADEOLAB, Via G.A. Amadeo 42, 20133 Milan, Italy

[‡]IFOM The FIRC Institute of Molecular Oncology, Via Adamello 16, 20139 Milan, Italy

[§]Institute of Materials, Ecole Polytechnique Fédérale de Lausanne (EPFL), Lausanne CH-1015, Switzerland

[∥]Department of Chemistry, Laboratory of Advanced Materials, Fudan University, Shanghai 200433, China

[⊥]Laboratory of Experimental Imaging, Fondazione IRCCS Istituto Neurologico Carlo Besta, Via Celoria 11, 20133 Milan, Italy

[#]Laboratory of X-ray Diffraction, École Polytechnique Fédérale de Lausanne (EPFL), Lausanne, CH-1015, Switzerland

[▽]Laboratory for Quantum Magnetism, École Polytechnique Fédérale de Lausanne (EPFL), Lausanne, CH-1015, Switzerland

S *Supporting Information*

ABSTRACT: Nanoparticle-based magnetic resonance imaging T_2 negative agents are of great interest, and much effort is devoted to increasing cell-loading capability while maintaining low cytotoxicity. Herein, two classes of mixed-ligand protected magnetic-responsive, bimetallic gold/iron nanoparticles (Au/Fe NPs) synthesized by a two-step method are presented. Their structure, surface composition, and magnetic properties are characterized. The two classes of sulfonated Au/Fe NPs, with an average diameter of 4 nm, have an average atomic ratio of Au to Fe equal to 7 or 8, which enables the Au/Fe NPs to be superparamagnetic with a blocking temperature of 56 K and 96 K. Furthermore, preliminary cellular studies reveal that both Au/Fe NPs show very limited toxicity. MRI phantom experiments show that r_2/r_1 ratio of Au/Fe NPs is as high as 670, leading to a 66% reduction in T_2 relaxation time. These nanoparticles provide great versatility and potential for nanoparticle-based diagnostics and therapeutic applications and as imaging contrast agents.

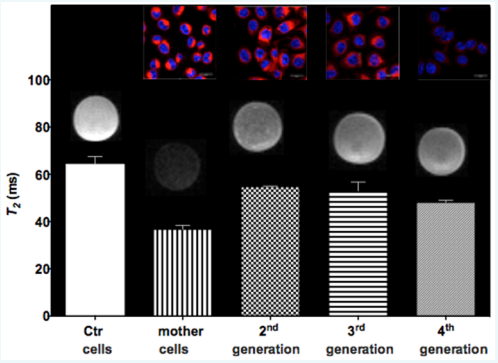

INTRODUCTION

Magnetic resonance imaging (MRI) is a powerful diagnostic technique primarily used to visualize fine morphological features of the human body with spatial resolution down to the submillimeter range, yielding valuable information on function and metabolism.[1] However, a limitation of MRI is its lack of sensitivity to relaxation times between normal and abnormal soft tissue, resulting in low contrast images. With the introduction of contrast agents in MRI, more specific and clear images can be obtained, providing physicians with sensitive and substantial diagnostic information.[2]

More recently, molecular and cellular MRI has been intensively studied to visualize and track target cells in living organisms, for example, to verify homing or engraftment of transplanted stem cells.[3] In order to provide a characteristic difference in MRI signal intensity, cells must be prelabeled with MRI contrast agents in vivo or in vitro. Nanostructured contrast agents based on both superparamagnetic iron oxides (SPIONs, T_2 negative agents) and paramagnetic chelates (Gd^{3+} and Mn^{2+}, T_1 positive agents) have been used for this purpose.[4] When prelabeling cells in vitro, the challenge is to induce sufficient cellular uptake of the contrast agent without affecting normal cellular functions. In addition, cells should retain the contrast agent for a time sufficient to provide useful information by MRI, which could range from few minutes or hours for imaging to weeks for cell tracking.

The efficiency of nanoparticle uptake by cells is directly influenced by the properties of the particle surface.[5−7] Extensive research has focused on increasing cellular uptake by surface modification strategies, such as conjugation of cell-penetrating peptides,[8] combination with transfection agents,[9] and encapsulation with dendrimers.[10] However, challenges still remain in

Special Issue: Interfacing Inorganic Nanoparticles with Biology

Received: October 6, 2016
Revised: November 6, 2016
Published: November 8, 2016

DOI: 10.1021/acs.bioconjchem.6b00577
Bioconjugate Chem. 2017, 28, 161−170

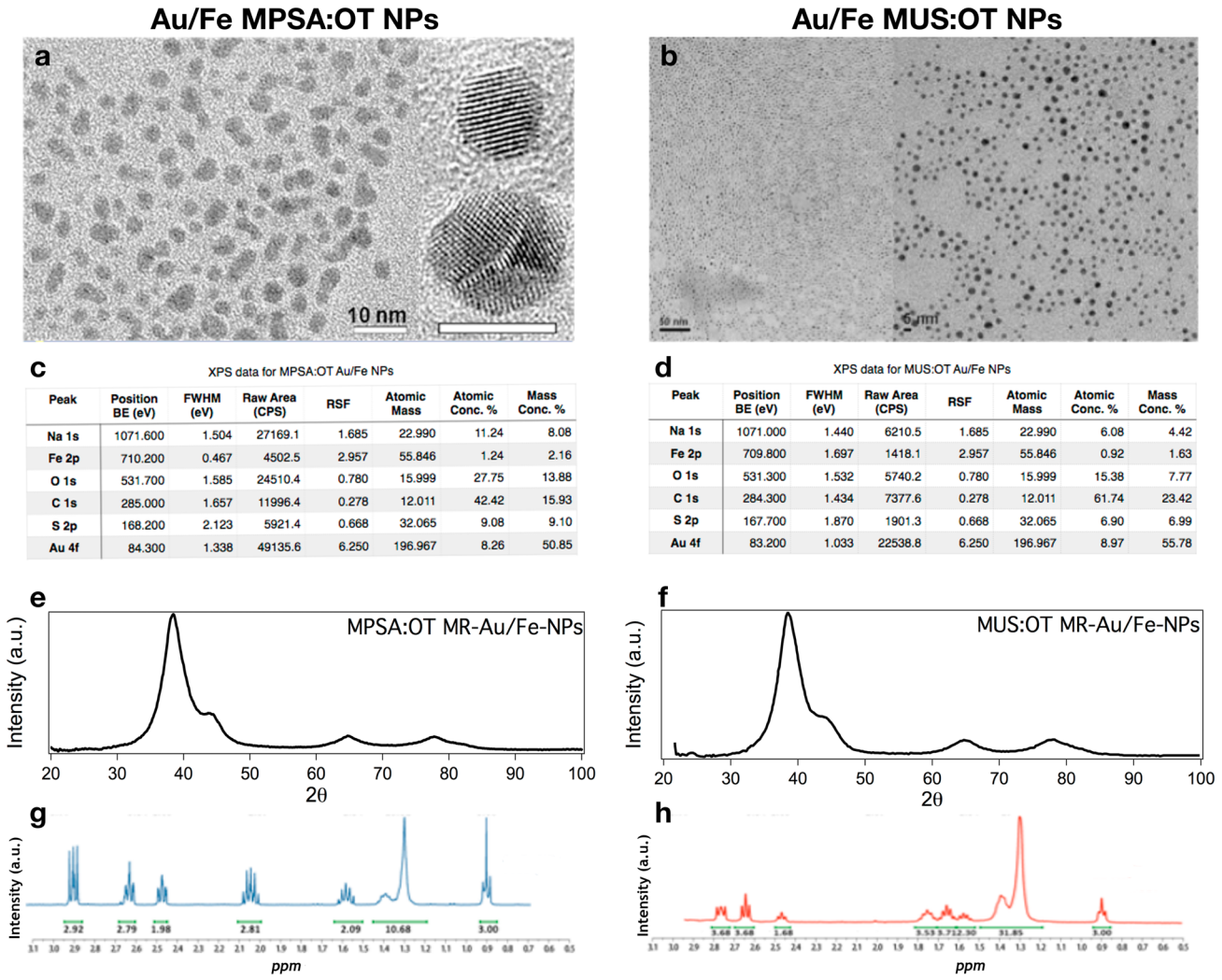

Peak	Position BE (eV)	FWHM (eV)	Raw Area (CPS)	RSF	Atomic Mass	Atomic Conc. %	Mass Conc. %
Na 1s	1071.600	1.504	27169.1	1.685	22.990	11.24	8.08
Fe 2p	710.200	0.467	4502.5	2.957	55.846	1.24	2.16
O 1s	531.700	1.585	24510.4	0.780	15.999	27.75	13.88
C 1s	285.000	1.657	11996.4	0.278	12.011	42.42	15.93
S 2p	168.200	2.123	5921.4	0.668	32.065	9.08	9.10
Au 4f	84.300	1.338	49135.6	6.250	196.967	8.26	50.85

Peak	Position BE (eV)	FWHM (eV)	Raw Area (CPS)	RSF	Atomic Mass	Atomic Conc. %	Mass Conc. %
Na 1s	1071.000	1.440	6210.5	1.685	22.990	6.08	4.42
Fe 2p	709.800	1.697	1418.1	2.957	55.846	0.92	1.63
O 1s	531.300	1.532	5740.2	0.780	15.999	15.38	7.77
C 1s	284.300	1.434	7377.6	0.278	12.011	61.74	23.42
S 2p	167.700	1.870	1901.3	0.668	32.065	6.90	6.99
Au 4f	83.200	1.033	22538.8	6.250	196.967	8.97	55.78

Figure 1. Physicochemical characterization of MPSA:OT Au/Fe NPs and MUS:OT Au/Fe NPs. (a, b) TEM images of MPSA:OT Au/Fe NPs (left, with high resolution TEM insert, scale bar for HR-TEM insets: 5 nm) and MUS:OT Au/Fe NPs (right). (c, d) XPS data for MPSA:OT Au/Fe NPs (left) and MUS:OT Au/Fe NPs (right). (e, f) XRD powder diagrams for MPSA:OT Au/Fe NPs (left) and MUS:OT Au/Fe NPs (right). (g, h) NMR analysis of surface composition of etched NPs, MPSA:OT Au/Fe NPs (left) and MUS:OT Au/Fe NPs (right).

achieving biological functionality as well as low toxicity, water solubility, and stability in biological media.

Many recent studies report on the synthesis and MRI potential of Au-coated iron oxide nanoparticles[11] and Au/Fe bimetallic and alloy nanoparticles.[12−16] Both solutions lead to superparamagnetic nanoparticles with contrast agent capability that in addition present an exposed, inert, noble metal surface. The presence of Au provides two main advantages: (i) a well-known and versatile platform for surface functionalization, the gold−thiol chemistry, and (ii) gold adds plasmonic features to the superparamagnetic NPs that can be exploited for multimodal imaging, such as contrast for CT (computed tomography) and SERS (surface enhanced Raman spectroscopy) imaging in vivo,[13] and photothermal therapy.[17]

Our primary motivation is to develop magnetic nanoparticles that can be used as nontoxic, cell-degradation resistant MRI contrast agents, e.g., for long-term follow-up studies of transplanted stem cells or for in vitro and in vivo studies to follow tumor growth of NP-loaded tumor cells. The magneto-responsive Au/Fe NPs described in this work combine the capability of cell internalization shown by mixed-ligand gold nanoparticles[5,18,19] with magnetic features.

A number of different methods have been previously reported for the preparation of bimetallic Au/Fe alloy nanoparticles,[13−15,20−26] core−shell or dumbbell nanoparticles,[27,28] with protocols including thermal decomposition,[15,23] pulsed laser deposition,[29,30] microemulsion techniques,[16,31] thermal vaporization,[32,33] laser-assisted synthesis in solution,[13,20] and aqueous reduction by borohydride derivates.[14] Chemical reduction of metal ions by sodium borohydrides has previously been used to prepare nanocrystalline magnetic materials, nanoalloys, and amorphous metals.[34,35] In this work, we report a new two-step synthesis to prepare magneto-responsive gold/iron nanoparticles (Au/Fe NPs) with two mixed-ligand coatings, either mercaptopropionylsulfonic acid:-octanethiol (MPSA:OT) or mercaptoundecylsulfonate:octanethiol (MUS:OT). Structural characterization and elemental analysis demonstrate that the resulting bimetallic nanoparticles have an average diameter of 4 nm (MPSA:OT, 4.0 ± 1.3 nm; MUS:OT, 4.0 ± 1.0 nm) with an average atomic ratio of Au to Fe of 7 (MPSA:OT) and 8 (MUS:OT), which enables Au/Fe NPs to be superparamagnetic at room temperature, with a blocking temperature of 56 K (MPSA:OT) and 96 K (MUS:OT), depending on the coating. Their high r_2/

DOI: 10.1021/acs.bioconjchem.6b00577
Bioconjugate Chem. 2017, 28, 161−170

r_1 ratio demonstrates their capability to be used as MRI T_2 contrast agents. Furthermore, we confirm their ability to penetrate cells and to be accumulated without apparent toxicity and to be retained in cells after cellular division up to the fourth generation. This combination of properties demonstrates the applicability of these nanoparticles as ideal MRI contrast agents.

RESULTS AND DISCUSSION

Synthesis and Physicochemical Characterization of Au/Fe Nanoparticles. We present a two-step method, which employs mild condition and is very easy to scale up. The synthesis of gold/iron nanoparticles (Au/Fe NPs) is performed in two steps in order to overcome the difference in the redox potential of iron and gold, as in most reducing conditions gold is reduced before iron. Therefore, the iron salts are first reduced to Fe_2O_3 by quickly adding a mixture of ferric (Fe^{3+}) and ferrous (Fe^{2+}) salts into an excess of $NaBH_4$ solution.

The reaction is very fast (less than a minute) and allows for high yields of the precursor iron complex. In the second step, the Fe precursor is mixed with gold salts and capping ligands and reduced with $NaHB_4$ to produce ligand-shell stabilized Au/Fe NPs, following a well-established gold nanoparticle synthesis procedure.[36] Our bimetallic Au/Fe-NPs are passivated by a mixed ligand monolayer composed either by MPSA:OT or by MUS:OT mixtures. MPSA and MUS are hydrophilic molecules that phase-separate into patches on the gold surface when forming mixed ligands monolayer with hydrophobic moieties like OT.

MPSA:OT Au/Fe NPs are a useful benchmark system to compare with published reports on Au/Fe alloy nanoparticles with pure MPSA coating.[14] Compared to those reports, our NPs are obtained with a method independent of thermal decomposition or the presence of an organic surfactant, which can be difficult to remove and may cause cellular toxicity.[37] Moreover, our Au/Fe NPs present a mixed ligand surface that has proven to be highly biocompatible in similarly prepared pure gold NPs. Indeed, our group previously investigated gold nanoparticles coated with an alternate arrangement of hydrophobic and longer hydrophilic sulfonated moieties (MUS), showing in both in vitro and theoretical models a high capability to penetrate into cells.[5,18,19]

Transmission electron microscopy (TEM) images reveal that the average diameter of MPSA:OT Au/Fe NPs is 4.0 ± 1.3 nm (Figure 1a). Similar results are obtained for MUS:OT Au/Fe NPs (Figure 1b), with a similar size distribution centered at 4.0 ± 1.0 nm. In bright-field mode of TEM, pure gold phases normally appear much darker than pure iron phases because of much higher proton number in gold atoms. Therefore, both Fe/Au core/shell NPs and phase-separated Fe and Au NPs are showing different contrast between the two phases in TEM images.[38] For example, both large scale (Figure 1a) and high-resolution (Figure 1a, inset) images of MPSA:OT Au/Fe NPs show homogeneous contrast, as other solid solution of Fe in Au NPs and alloyed Au/Fe NPs.[14] These kinds of peculiar bimetallic NPs where Fe is homogeneously distributed in the fcc crystal of gold core allow for the design of small-size contrast agent NPs (compared to core−shell design) that maintain plasmonic and magnetic properties.[12,13,21,38,39] High-resolution TEM images also reveal that MPSA:OT Au/Fe NPs have multiple twinned boundaries of AuFe, single-crystal and other crystal structures, substantially in a similar fashion as for 4 nm pure Au NPs observed by others.[38] These results, in addition to X-ray powder diffraction (XRD), reveal that the nanoparticle core (in both MPSA:OT and MUS:OT Au/Fe NPs) presents iron oxides, as well as with a slight degree of alloying with gold, thus supporting the presence in the core of both iron and gold and the protective effect of the gold lattice on the iron component.

The iron precursor shows the presence of crystalline iron oxides (Supporting Information, Table S1a,b) of ∼2 nm in size. MPSA:OT and MUS:OT Au/Fe NP core lattice parameters (4.0698 and 4.0681 Å, respectively, as estimated via Scherrer's formula; see Supporting Information Table S1b) show some relaxation compared to the crystal lattice of pure gold (lattice constant reported in the literature: 4.0782(5) Å[14−16,31,40]). This suggests a slight degree of alloying, similar to previous reports.[14−16,31,40] The corresponding peaks of iron and gold, reported in Figure 1e and Figure 1f, are analyzed and are in good agreement with reported values.[14−16,31,40] The lattice parameters of bulk Au/Fe alloys have been characterized in a wide range of compositions, for example, 3.3% Fe (4.0690 Å) and 20% Fe (3.995 Å).[41] Application of Vegard's law in this range allows for an estimation of the iron composition from the lattice parameter, which results in 10.3% Fe for MPSA:OT Au/Fe NPs and 12.3% Fe for MUS:OT Au/Fe NPs.

By X-ray photoelectron spectroscopy (XPS), the average atomic ratio of MPSA:OT Au/Fe NPs is found to be around 7 (14.3% Fe). The value is in agreement (within experimental error) with the data obtained from XRD analyses and from EDS (energy dispersive X-ray spectroscopy, as reported in Supporting Information Figure S2). In this ratio region, Fe atoms occupy face-centered cubic (fcc) sites of Au atoms.[42] Furthermore, the particle surface must be dominated by Au atoms to avoid Fe oxidation, which is similar to small sized iron−platinum (FePt) nanoparticles with Pt segregation on the surface.[38,43] The presence of gold on the surface of Au/Fe NPs ensures that they have the same surface properties as pure gold NPs. It should be pointed out that the ratio of Fe to Au is not identical for each single NP, and we provide an average number for the nanoparticle population. Similar results are obtained for MUS:OT Au/Fe NPs where the average atomic ratio of Au/Fe is found to be around 8 (12.5% at. Fe), again in the range of fcc arrangement of Fe and Au atoms.[42] In both cases, XPS data show also the coexistence of S^{5+} and S^{2-} oxidation states on the surface of NPs (Figure 1c,d), which represent the sulfonate groups of MPSA or MUS, and the thiol groups of MPSA, MUS or OT, respectively.[44]

Surface monolayer composition is further confirmed by NMR. For the composites, two ^{1}H NMR peaks of Au/Fe NP postetching solutions are compared directly (Figure 1g): the $-CH_3$ peak of OT at 0.90 ppm and the $-CH_2$ adjacent to the sulfonate of MPSA or MUS at 2.95 ppm. The MPSA:OT ratio is 1.46:1. FTIR results (Supporting Information Figure S3) support the finding of the coexistence of MPSA and OT on the surface of Au/Fe NPs. The ligand ratio for MUS:OT Au/Fe NPs is 1.84:1, as determined by NMR (Figure 1h). The ξ-potential of Au/Fe NPs dispersed in water is measured to be −25 ± 1 mV for MPSA:OT NPs and −28 ± 4 mV for MUS:OT NPs; thus they are anionic and exhibit excellent colloidal stability. Furthermore, the Au/Fe NPs retain the localized surface plasmon resonance (LSPR) characteristic of pure Au NPs, as evidenced by a lack of attenuation or shift in the position of Au/Fe NPs' plasmon peak (Supporting Information Figure S1c). This is in agreement with similar properties of low-iron content, chemically synthesized Au−Fe alloy NPs,[14,23,45,46] which also show insignificant shift in the

DOI: 10.1021/acs.bioconjchem.6b00577
Bioconjugate Chem. 2017, 28, 161−170

position of LSPR peaks compared to pure gold NPs, as the low content in Fe does not modify substantially plasmonic properties. This is also supported by our high resolution TEM results, as the crystal structure of the Au/Fe NPs does not point to phase separations of Au and Fe in the NPs core.

Magnetic Properties. Magnetic properties of Au/Fe NPs are measured using a SQUID magnetometer (Figure 2a,b for MPSA:OT Au/Fe NPs, Figure 2c,d for MUS:OT Au/Fe NPs). Magnetic hysteresis loops at different temperatures indicate that Au/Fe NPs are superparamagnetic at room temperature. The zero-field-cooled (ZFC) and field-cooled (FC) curves show the blocking temperatures (T_B) of Au/Fe NPs to be 56 K for MPSA:OT Au/Fe NPs (Figure 2b) and 96 K for MUS:OT Au/Fe NPs (Figure 2d). As compared to iron and iron oxide nanoparticles of the same size, these Au/Fe NPs have similar blocking temperature but a smaller magnetization, which is mainly contributed by the small Fe portion and its wide distribution.

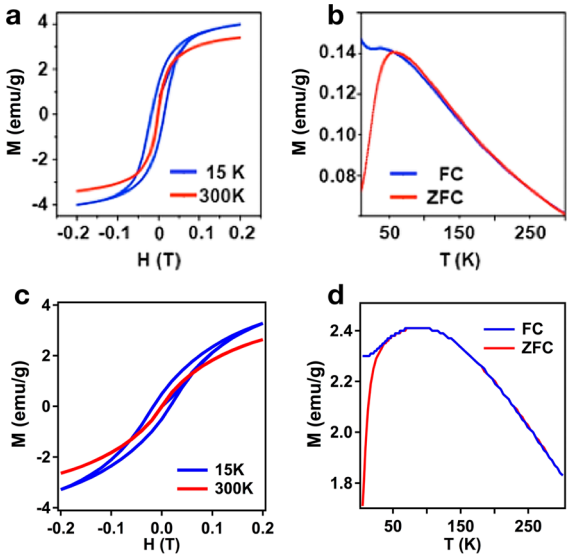

Figure 2. Magnetic properties of Au/Fe NPs: (a) magnetic hysteresis loop for MPSA:OT Au/Fe NPs; (b) zero-field-cooled (ZFC) and field-cooled (FC) for MPSA:OT Au/Fe NPs; (c) magnetic hysteresis loop for MUS:OT Au/Fe NPs; (d) zero-field-cooled (ZFC) and field-cooled (FC) for MUS:OT Au/Fe NPs.

The potential for deployment of these NPs as effective contrast agents in MRI is assessed through phantom experiments and in vitro MRI. The specific relaxivity (r_2) and the ratio r_2/r_1 are the figure-of-merit for T_2-weighted contrast agents, such as iron oxide nanoparticles. The higher is the r_2/r_1 ratio, the better is the contrast efficiency. To examine the contrast characteristics of Au/Fe NPs as a MRI contrast agent, we acquire the T_2-weighted images (Figure 3a, MPSA:OT; Figure 3c, MUS:OT Au/Fe NPs), and T_1, T_2 relaxation times of the NPs dispersion in water. The measurements are carried out with a 7.0 T preclinical MRI scanner. The transverse relaxation rate R_2, which is the reciprocal of the T_2 relaxation time, is calculated from the MR images of MPSA:OT (Figure 3a) or MUS:OT (Figure 3c) Au/Fe NPs at different concentrations. Data in Figure 3 show the correlation between the R_1, R_2 relaxation rate and the concentration of iron in MPSA:OT (Figure 3b) and MUS:OT (Figure 3d) Au/Fe NPs. The specific relaxivity ($r_{1,2}$, mM^{-1} s^{-1}) measures the change in the relaxation rate per unit concentration of iron. In particular,

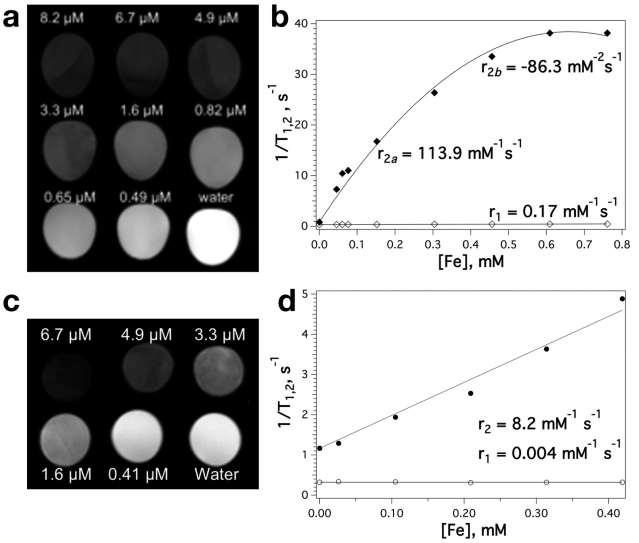

Figure 3. MRI properties of Au/Fe NPs. On the left, the magnetic resonance images of agar phantoms containing (a) water dispersion of MPSA:OT Au/Fe NPs or (c) of MUS:OT Au/Fe NPs. On the right, the specific relaxivity of (b) MPSA:OT Au/Fe NPs or (d) of MUS:OT Au/Fe NPs.

the specific relaxivity r_2 (mM^{-1} s^{-1}) represents the relaxation rate (R_2) enhancements (relative to pure water) of the nanoparticle suspension as a function of the Fe ion concentration. Usually, $r_{1,2}$ is obtained from the plot using the equation $R_{1,2} = 1/T_{1,2} = (1/T_{1,2})_0 + r_{1,2}C$, where $R_{1,2}$ is the relaxation rate of the aqueous solution of nanoparticles, $(T_{1,2})_0$ is the relaxation time in absence of nanoparticles, and C is the concentration (mM) of iron.[47]

This equation allows for a univocal parameter r to be extracted and compared among samples. This equation is well applied to r_1 of MPSA:OT and both r_1 and r_2 of MUS:OT NPs. However, MPSA:OT Au/Fe NPs show a nonlinear behavior in the presented Fe concentration range. Our R_2 data for MPSA:OT Au/Fe NPs, indeed, span a larger range of Fe concentrations and follow below 0.4 mM Fe content a linear regime to reach saturation in the range 0.4−0.8 mM Fe. By analyzing data with a quadratic polynomial of the kind $R_2 = R_0 + r_{2a}C + r_bC^2$, where R_{2b} is the relaxation rate of the aqueous NP solution, $R_0 = 1/(T_2)_0$ is the inverse of the relaxation time in absence of nanoparticles, and C is the concentration (mM) of iron, we can explain both behaviors. The high slope in the linear regime (r_{2a} = 113.9 mM^{-1} s^{-1}) is related to the positive contribution of C until a turning point, highlighted by the negative r_{2b} value (r_{2b} = −86.3 mM^{-2} s^{-1}), is reached at ($r_{2a}/2$) r_{2b} = 0.66 mM Fe. Then, the high NP concentration may favor different exchange rates of the protons that contribute to the MR signal so that at higher NPs concentration those protons may have unequal access to the paramagnetic centers.

The phantom experiments in Figure 3a and Figure 3c show that both nanoparticles induce a hypointense signal in a concentration-dependent manner on the T_2-weighted images. R_2 relaxation time increased significantly from 0.49 μM to 8.2 μM (6.7 μM for the MUS:OT) Au/Fe NP concentrations. The contrast of Au/Fe NPs suspensions is shown in the phantom experiments where a strong reduction of the signal intensity in T_2-weighted images is observed (Figure 3a, Figure 3c). The absolute value of r_1 and r_2 of Au/Fe NPs is low because of the small Fe portion and wide distribution. However, the unique

DOI: 10.1021/acs.bioconjchem.6b00577
Bioconjugate Chem. 2017, 28, 161−170

surface structure of Au/Fe NPs allows dramatic increase of the r_2/r_1 ratio. This behavior can be explained by the interplay of two main effects. First, the segmented regions of hydrophilic $-SO_3^-$ groups in the NP's biligand shell may be capable of trapping large amounts of "icelike" water,[48] resulting in a larger r_2 relaxivity.[49] Second, the hydrophobic pure Au layer surface of the NPs may efficiently block the external water molecules from interacting with the Fe magnetic core, inducing a large decrease in the spin−lattice r_1 relaxivity.[50] The r_2/r_1 ratio value is as high as 670 (for MPSA:OT Au/Fe NPs: r_{2a}/r_1) and leads to a marked reduction in T_2 relaxation time, further supporting the potential of Au/Fe NPs as MRI T_2 contrast agents. Indeed, the efficiency parameter r_2/r_1 is above 10^2 at field of 1.41 T (in the range of clinically relevant field intensity, 1.5 T), where most negative contrast agents have a threshold value just above 2 [12,13,21,39] (as compared to commercially available SPIONs:[12,13,21,39] Endorem, 6.56, and VOSP, 2.35).

Cellular Uptake and Cell Viability. BODIPY-labeled nanoparticles are used to evaluate and quantify cellular internalization through a series of fluorescence activated cell sorting (FACS) and confocal laser scanning microscopy (CLSM) studies. Figure 4 summarizes the in vitro results for

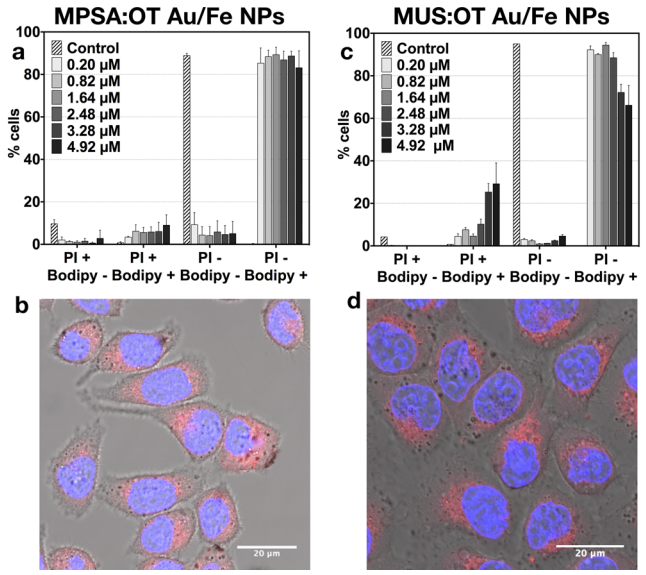

Figure 4. Cellular uptake of Au/Fe NPs. FACS measurement of NP toxicity with increasing NP concentration for MPSA:OT Au/Fe NPs (a) and MUS:OT Au/Fe NPs (c). CLSM images illustrating cytosolic NP uptake at 37 °C for MPSA:OT Au/Fe NPs (b) and MUS:OT Au/Fe NPs (d). NPs were prelabeled with BODIPY (red) for fluorescence detection. Nuclei were counterstained with Hoechst 33342 (blue). Larger micrographs for MPSA:OT and MUS:OT Au/Fe NPs loaded cells are reported in Supporting Information Figure S4.

MPSA:OT and MUS:OT Au/Fe NPs. A dose−response study is conducted by FACS analysis of cell viability, and the results are represented in Figure 4a,c (FACS dot plots are reported in Supporting Information Figures S5 and S6). Propidium iodide (PI) is a nonpermeant cell dye and is excluded by intact cell membranes of live cells, while dead or damaged cells allow dye entry and are stained by PI. Therefore, the percentage of PI positive, BODIPY positive cells is an indication for NP-induced cell mortality. The percentage of PI negative, BODIPY-positive cells reflects the percentage of cells that have uptaken the NPs without effect on their viability. Cells are viable (viability above 80%) after the uptake of Au/Fe NPs at tested concentrations. MUS:OT NPs show a slightly higher toxicity at the highest tested concentration as compared to the MPSA:OT NPs; however viability is well above 60% even at high doses (3.28 and 4.92 μM). The highest concentration (4.92 μM), indeed, represents a high dose of nanomaterial, while at concentration reasonable for in vivo applications (such as the one used for the confocal and MRI images, 1.64 μM) viability is above 80% for all NPs. These data are confirmed by LDH (lactate dehydrogenase) leakage test (Supporting Information Figure S7). Cells that lose the integrity of the plasma membrane due to perforation or necrosis release the cytosolic enzyme LDH in the medium or extracellular space. For NP concentration between 0.05 and 0.4 mg/mL (0.4−3.24 μM), we can see that LDH release at 4 h is equal to or lower than that of the control at all concentrations. At 24 h, LDH release at the maximum concentration is about 3 times higher than control. After 48 h of NPs incubation, LDH release reaches a plateau at 0.1 mg/mL and above (0.82 μM) with an LDH release that is about 2.5 times higher than control. These results are promising, as a high cell loading with NPs can be achieved with shorter incubation time (up to 24 h) while keeping cytotoxicity low.

We also observed that the more hydrophobic MPSA:OT NPs tend to aggregate with time at very high concentrations. Possibly, this higher tendency of MPSA:OT NPs to form larger cluster in medium over time reduces the uptake of smaller particles, masking toxicity at higher doses, compared to MUS:OT NPs.

One limitation of FACS analysis is that it does not discriminate between cellular internalization and adsorption to the cell surface. For this reason, complementary CLSM imaging studies are carried out to confirm that the nanoparticles are present into the cytosol. HeLa cells are incubated with either type of NPs for 4 h at 37 °C. The overlay of the bright-field and fluorescence images clearly shows that HeLa cells internalize BODIPY-labeled Au/Fe NPs. We can exclude that free BODIPY is responsible for the signal, as we ensured the absence of unbound dye by a test developed by our laboratory[51] (data not shown). The diffuse high fluorescence intensity signal in the cytosol, for both MPSA:OT and MUS:OT NPs (see Figure 4b, Figure 4d), indicates the homogeneous distribution of NPs in contrast to a spotty appearance typical of when NPs enter solely via endocytosis. This can be attributed to NP uptake both by endocytosis and by passive membrane diffusion. By preferring NP entry passively into the cytosol of the cells over classic active endocytic mechanisms, the NPs can be protected from (i) degradation in the metal-dissolving acidic conditions along the endocytic/lysosomal pathways[52] and (ii) expulsion from the cells. Hence, passive uptake is beneficial for long-term follow-up in applications such as stem cell loading for post-transplant tracking. Detailed studies on the mechanisms of entry and uptake are ongoing and will be the subject of a future paper.

MRI Imaging of Au/Fe NPs-Loaded Cells. To assess the imaging potential of the NPs, MR imaging of cells labeled with NPs are performed to quantify the T_2 relaxation time. MRI T_2-weighted images of the cells labeled with nanoparticles showed an evident hypointensity (Figure 5a) corresponding to a reduction in T_2 relaxation time when compared to the control cells. Magnetic iron-containing nanoparticles such as our Au/Fe NPs create a local perturbing field that leads to a marked shortening on proton relaxation time (T_2 relaxation time) in MRI process giving a negative signal.[47,53]

DOI: 10.1021/acs.bioconjchem.6b00577
Bioconjugate Chem. 2017, 28, 161−170

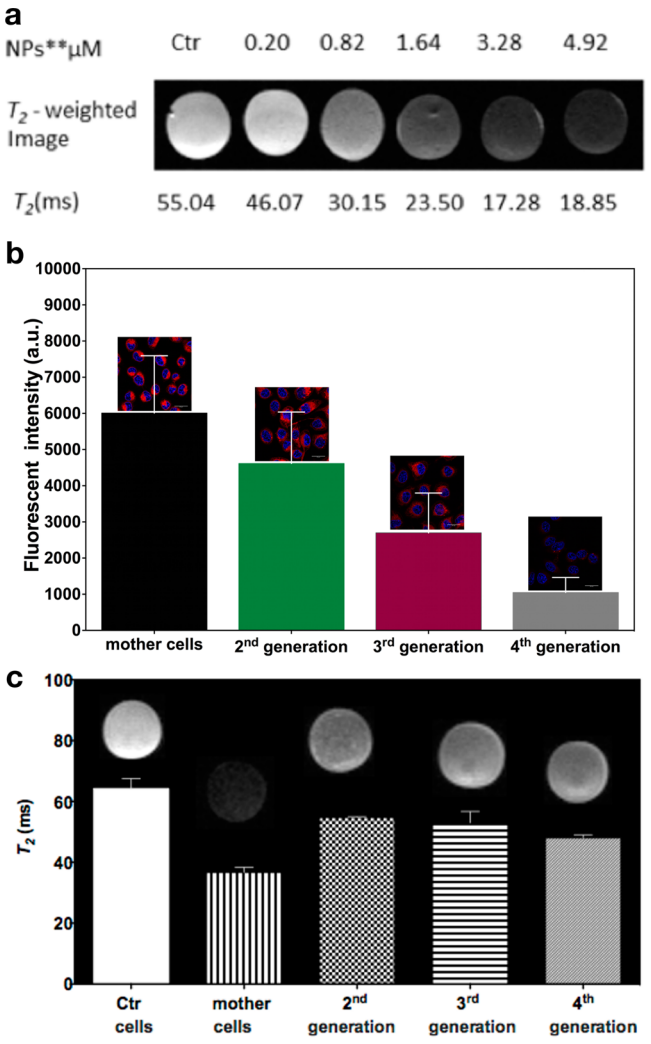

Figure 5. Effectiveness of MPSA:OT Au/Fe NPs as MRI imaging probe on NPs-loaded cells. (a) MRI imaging of NPs-loaded cells as a function of NPs concentration (the values refer to the concentration administered to the cells). (b) CLSM images and quantification of cytoplasmatic fluorescence signal from BODIPY-labeled MPSA:OT Au/Fe NPs as a function of dilution upon subsequent cell divisions and generations. The disappearance of the NPs (fluorescent red signal) from the cells is due to dilution following cellular division. The fluorescence signal can be detected up to the fourth generation. (c) MRI signal as a function of dilution upon cell division in subsequent generations, with untreated control cells as a reference signal. Error bars represent one standard deviation from the mean.

Figure 5a shows a reduction in T_2 relaxation time as the NP concentration increases after 8 h of incubation. A total reduction of 66% in T_2 relaxation time is achieved for the highest concentration when compared to the control cells.

Monitoring Au/Fe NPs Concentration in Dividing Cells. In perspective of the potential future use as long-term or even permanent cell stain, the dependence of NP detection limit in cell generations is an important parameter. We therefore followed the NPs signal in subsequent cell divisions. For both fluorescence and MRI experiments, the number of cells analyzed is kept constant at each generation step, so to follow the dilution of the BODIPY-MPSA:OT Au/Fe NPs. We expect that upon cell division, the internalized NPs are divided between the mother and the daughter cells, diluting the fluorescence and MR signals.

CLS micrographs (Figure 5b) show that the HeLa cells retain a significant amount of BODIPY-MPSA:OT Au/Fe NPs after several generations. These NPs are detected after cell division up to the fourth generation. It is noteworthy that these NPs do not affect cell division or metabolism, while the growth rate is reportedly reduced by other magnetic nanoparticles agents.[5,18,19,54]

More importantly, these results are confirmed by MRI. Indeed we were able to detect the NPs in daughter cells, in similarly prepared samples (Figure 5c). Although fluorescence is clearly more sensitive to diluted concentrations, our Au/Fe NPs, compared to untreated cells, continue to show a good contrast in MRI even upon dilution in subsequent generations. This fact, together with the findings about the low toxicity and limited interference with cell viability, supports the use of these nanoparticles for MRI visualization in vivo. We are indeed already investigating their usefulness for research on metabolic activity and differentiation of the transplanted stem cells and for studies of tumor progression in 3D cell culture of NP-loaded tumoral cells (manuscripts in preparation).

CONCLUSIONS

We have described a simple and novel way for synthesizing stable magnetically responsive bimetallic gold/iron nanoparticles and have demonstrated their high potential as MR imaging contrast agents with high r_2/r_1 ratio. The presence of gold as a passivating layer prevents the oxidation of iron, thereby increasing the stability of the magnetic nanoparticles, and furthermore offers access to the versatile functionalization scheme of thiols on gold. The labeling of the Au/Fe NPs with a biocompatible monolayer and their retention in the cytosol pave the way for numerous biomedical applications, such as stem cell tracking by MRI and follow-up of cell therapy. A significant advantage of this synthesis is that it can be used as basis to design other nanoparticles by changing certain parameters. Nanoparticle diameter and magnetic properties can be tuned by changing the gold to iron ratio, and surface ligands can be exchanged or conjugated with biomolecules (e.g., antibodies, peptides, or proteins) to achieve target-directed MRI or imaging multimodality. Thus, these nanoparticles and their synthesis offer great versatility and potential for nanoparticle-based diagnostics, therapeutic applications, and imaging contrast agents.

EXPERIMENTAL PROCEDURES

Synthesis of Gold/Iron Nanoparticles (Au/Fe NPs). A summary of the nanoparticles used in this study is presented in Table 1. Magneto-responsive Au/Fe NPs were prepared as follows. First, iron complexes are synthesized by chemical reduction before subsequent mixing with gold salts for preparation of Au/Fe NPs. For the preparation of iron complexes, a mixture of ferrous and ferric ions ($FeCl_3 \cdot 6H_2O$ (1.24 g) and $FeCl_2 \cdot 4H_2O$ (0.64 g) in 4 mL of acidic water) is

Table 1. Descriptions, Abbreviations, and Compositions of the Nanoparticles Designed for This Study

nanoparticle (abbreviation)	core type (diameter)	ratio of ligands (detected ratio)
gold/iron MPSA:OT (MPSA:OT Au/Fe NPs)	Au/Fe (4.0 ± 1.3 nm)	MPSA:OT 2:1 (1.46:1)
gold/iron MUS:OT (MUS:OT Au/Fe NPs)	Au/Fe (4.0 ± 1.0 nm)	MUS:OT 2:1 (1.84:1)

DOI: 10.1021/acs.bioconjchem.6b00577
Bioconjugate Chem. 2017, 28, 161−170

added very quickly, and with vigorous stirring, to a sodium borohydride ($NaBH_4$) solution in large stoichiometric excess (1 g in 150 mL of ethanol). The reaction is carried out under nitrogen atmosphere at room temperature. The reaction solution becomes black, resulting in a fine black precipitate that is further filtered and washed with ethanol. The final Au/Fe NPs are prepared by adapting an existing procedure.[5] The prepared iron complex (100 mg) is added to $NaBH_4$ solution (1 g in 150 mL of ethanol) and sonicated for 1 h. The resulting dispersion is added dropwise (over a period of 1 h) to 0.9 mmol of gold salt ($HAuCl_4$) in 200 mL of ethanol and 0.9 mmol of thiolated ligands. The ligand solution consists of a mixture in 2:1 molar ratio of sulfonated to hydrophobic thiol, either MPSA:OT 2:1 or MUS:OT 2:1. The reaction is carried out under N_2 atmosphere and stirred for 3 h. The resulting particles are stored overnight at 4 °C, then collected by filtration, washed 3 times (by ethanol, methanol, and acetone), and finally dried under vacuum. The dried black powder can be attracted by a magnet and redispersed into water (Supporting Information Figure S1a,b) for subsequent experiments.

Fluorescent Labeling of Nanoparticles. For the cell experiments, nanoparticles are labeled with BODIPY 650/665 nm (hereafter referred to as BODIPY) (Invitrogen, OR, USA) according to the protocol described by Verma et al.[5] The complete removal of free BODIPY after washing the labeled nanoparticle preparation is assessed according to the protocol in Andreozzi et al.[51]

Nanoparticle Characterization. The absorption spectra of NP suspensions are recorded on a UV−vis spectrophotometer (Ultrospec 2100*pro*, Amersham Bioscience). NP surface charge is approximated by measuring the ζ potential using a Zetasizer Nano ZS (Malvern Instruments, Malvern, U.K.). The results are expressed as ζ potential (mV) ± 1 standard deviation (SD). NP size is measured by transmission electron microscopy (TEM). TEM analysis is performed with a Philips/FEI CM300 transmission electron microscope at 300 kV with an energy dispersive X-ray spectrometer (EDS) attached. X-ray photoelectron spectroscopy (XPS) spectra are acquired by using Kratos AXIS Ultra. Fourier transform infrared spectroscopy (FTIR) spectra are measured on a JACSO FT/IR6320. Magnetic properties are characterized by using a superconducting quantum interference device (SQUID) magnetometer (Cryogenic).

^{1}H NMR measurements of ligand composites on the surface of NPs are carried out on a Bruker Avance 300 spectrometer operating at a frequency of 400 MHz after washing and etching. Generally, 30 mg of NPs and 25 mg of potassium cyanide (KCN) are dissolved in 1 mL of methanol. The solution is sonicated for 4 h and then left stirring overnight. Afterward the solution is filtered through a 0.2 μm membrane filter to remove any gold, iron, and other insoluble components and subsequently analyzed.

XRD (X-ray Diffraction). The samples are front-loaded as is into the well of a sample-holder from PANalytical (The Netherlands) hewn out of a silicon single crystal. Then powder diagrams are recorded on an MPD PRO system (PANalytical, The Netherlands) using an automatic divergence slit; at the end the diagrams are converted to a fixed DS of $^1/_2$°. The step-size is 0.008°, in the 2θ range 20−100°. The diagrams are then refined by the Rietveld method with the help of the FullProf program. The profile of the lines is described by means of a pseudo-Voigt function. The same parameters are refined for all samples. Finally, the sizes are computed by means of Scherrer's formula, based on the full widths at half-maximum evaluated by the FullProf program.

Cell Culture and Imaging. Human cervical carcinoma cells (HeLa) are grown in Dulbecco's modified Eagle medium (Gibco) supplemented with 10% heat inactivated fetal bovine serum (FBS), L-glutamine (2 mM), 0.1 mM nonessential amino acids (ThermoFischer Scientific), 1 mM sodium pyruvate, penicillin (100 U mL^{-1}), streptomycin (100 μg mL^{-1}). Cultures are incubated at 37 °C, 5% CO_2 and passaged regularly when reaching 70−80% confluence.

For CLSM studies, cells are seeded in a μ-Slide 8-well Ibidi plate (Martinsried, Germany) at a density of 5×10^4 cells per well and are allowed to adhere overnight. Before cell incubation with nanoparticles, the medium containing fetal bovine serum is replaced with serum-free medium to avoid nonspecific binding of NPs to serum proteins. Cells are then incubated with 1.64 μM NPs for 4 h at 37 °C. After incubation the cells are washed 3 times with PBS. For fluorescence imaging, NPs labeled with BODIPY[19,51] are added to the cells and the incubation is performed as above. Nuclei are counterstained with Hoechst 33342 (Invitrogen, OR, USA), according to the manufacturer's instructions. Cellular uptake and internalization of the fluorescently labeled NPs are visualized and evaluated with an inverted CLSM (Leica TCS SP2 confocal microscope equipped with a 63/1.4 NA oil-immersion objective, HCX PL APO 63X Lbd Bl, Leica Microsystems) employed for analysis, using excitation lines at 405 (Hoechst 33342) and 633 nm (BODIPY (650/665) nm). All images were collected at identical laser settings, and the basal fluorescence signal in the red channel of control samples is set as zero reference. ImageJ software is used for image analysis.

Cell Viability: FACS Analysis. HeLa cell incubation with BODIPY-labeled NPs, in the concentration range 0.20−4.92 μM (0.025−0.6 mg/mL; molarity conversion was obtained according to refs 19 and 55), is performed as described above. Cells without nanoparticles are used as control. After 4 h of incubation, 5×10^5 cells are collected by trypsination and washed with PBS containing 1% BSA. The staining of nonviable cells is performed with PI (75 μM in PBS) for 5 min at room temperature. The samples are analyzed immediately on a flow cytometer (FACSCanto II, BD Biosciences) with excitation at 488 nm for PI and an excitation at 633 nm for BODIPY. All experiments were performed in triplicates.

LDH Release Cytoxocity Test. 4000 cells/well were plated in 96-well plates. After 24 h, cells were treated with control solution and MUS:OT Au/Fe NPs at different concentrations for different times of incubation (4, 24, 48 h). After the incubation time, the supernatant was removed and the LDH reagent was added according to the manufacturer's instructions (Pierce LDH cytotoxicity assay kit, Thermofisher, Milan, Italy), and reaction was evaluated via absorbance measurements (490 and 680 nm) with a microplate reader (Tecan Infinite 200). A background control of NPs without LDH reagent was prepared to subtract NPs absorbance contribution at the wavelengths used.

MRI Measurements. MR images are acquired on a BioSpec 70/30 USR (Bruker, Ettlingen, Germany) preclinical MRI scanner. All measurements are done at room temperature. Acquisitions are performed on phantoms containing NPs dispersed in water at different concentrations (from 0.49 to 8.20 μM).

For in vitro MRI, cells are cultured and incubated with nanoparticles as described above. Cells are incubated with NPs

DOI: 10.1021/acs.bioconjchem.6b00577
Bioconjugate Chem. 2017, 28, 161−170

in a concentration range of 0.20−4.92 μM for 8 h at 37 °C. 2 × 10^6 nonlabeled or magnetically labeled cells are collected, centrifuged, and resuspended in 0.3 mL of 2% agar at approximately 60 °C and then chilled at 4 °C to allow the suspensions to solidify for MRI. All experiments were performed in triplicates. MR images are acquired on a BioSpec 70/30 USR (Bruker, Ettlingen, Germany) preclinical MRI scanner. The system has a magnetic field strength of 7 T and a 30 cm warm bore diameter. The scanner is equipped with an actively shielded gradient system with integrated shims set up to second order. The maximum gradient amplitude is 400 mT/m. MRI studies are carried out using a transceiver linear birdcage rf coil having a diameter of 72 mm. Preliminary 3-orthogonal plane gradient echo tripilot scan is used as a geometric reference for slice selection. T_2-weighted images are acquired using a rapid acquisition with relaxation enhancement (RARE) sequence with the following parameters: FOV 8 × 8 cm^2, matrix 256 × 256, slice thickness 4 mm, TR = 3500 ms, TE effective = 40 ms, rare factor = 4, in plane resolution = 312 μm^2, number of averages (NA) = 1.5 coronal contiguous slices are acquired in 3 min and 44 s. T_1, T_2, and T_2* relaxation times are also estimated. For T_1 we use a RARE sequence 122 1 with variable TR with the following parameters: FOV 4 × 4 cm^2, matrix 64 × 32, TR = (267, 500, 700, 1000, 1500, 2500, 7000, 10000 ms), TE effective = 20 ms, BW 45 kHz, in plane resolution = 625 × 1250 μm^2, NA = 2. Scan time was 18 min 46 s. For T_2 estimation, we use a multislice multiecho (MSME) sequence with variable TE. The sequence has the following parameters: FOV 4 × 4 cm^2, matrix 64 × 64, TR = 3500 ms, echo spacing = 10.5 ms, number of TE images = 20, BW 50 kHz, in plane resolution = 625 × 625 μm^2, NA = 10. Scan time is 28 min. For T_2* estimation a multigradient echo (MGE) is used with the following parameters: FOV 4 × 4 cm^2, matrix 64 × 64, TR = 2500 ms, minimum TE = 2.4, echo spacing = 1.28 ms, number of TE images = 80, flip angle = 30°, BW 50 kHz, in plane S2 resolution = 625 × 625 μm^2, NA = 10. Scan time is 20 min. For relaxometric studies, 3 axial slices are acquired with a slice thickness of 7 mm and an interslice distance of 14 mm. T_1, T_2, and T_2* relaxation times are estimated using Paravision 5.1 (Bruker, Ettlingen, Germany).

Monitoring Au/Fe NPs Concentration in Dividing Cells. HeLa cells are grown until 80% confluence in 10 cm Petri dishes, then incubated with nanoparticles in serum-free medium to a final concentration of 0.82 μM for 8 h. Controls are treated the same way but without the administration of NPs. Then, of the collected cells, 2 × 10^6 labeled and nonlabeled cells each are prepared for MRI analysis; 5 × 10^4 labeled and nonlabeled cells are plated in Ibidi round slides for CLSM imaging, and 2 × 10^6 labeled and nonlabeled cells are each recultured in fresh medium containing serum. For MRI, samples are prepared as already described for MRI in vitro experiment. The duplication time of HeLa cells in culture is 23−24 h. In order to follow the decrease in fluorescence and hence nanoparticle concentration, the cells are imaged by CLSM (as described above) and recultured every 24 h until no fluorescent signal is detected. All experiments were performed in duplicates, and for each replicate images of 10 different fields were recorded. All images were collected at identical laser settings. The quantitative analysis of fluorescent nanoparticle uptake is performed with MetaMorph 7.7 (2011 Molecular Devices) as reported.[19]

■ ASSOCIATED CONTENT

Supporting Information

The Supporting Information is available free of charge on the ACS Publications website at DOI: 10.1021/acs.bioconjchem.6b00577.

UV−vis, magnetic attraction photos, EDS, XRD, and FTIR data, FACS data plots, LDH cytotoxicity tests (PDF)

■ AUTHOR INFORMATION

Corresponding Authors

*E-mail: barbara.sanavio@istituto-besta.it.
*E-mail: francesco.stellacci@epfl.ch.

ORCID

Barbara Sanavio: 0000-0001-5837-4097
Francesco Stellacci: 0000-0003-4635-6080

Author Contributions

○F.S. and B.S. contributed equally.

Notes

The authors declare no competing financial interest.

■ ACKNOWLEDGMENTS

We thank Ahmet Bekdemir for supporting us during XRD measurements. This work was supported by Italian Ministry of Health Grant GR-2009-1579848. F.S. was partially funded by Investigator Grant IG 11723 from AIRC Foundation and by Besta5x1000. B.S. received support from fellowships on Italian Ministry of Health Grant GR-2009-1579848 and on EU *Theraglio* FP7-Health-2013-Innovation Grant 602923.

■ ABBREVIATIONS

CLSM, confocal laser scanning microscopy; CT, computed tomography; DLS, dynamic light scattering; FACS, fluorescence activated cell sorting; FTIR, Fourier transform infrared spectroscopy; MPSA, mercaptopropylsulfonic acid; MRI, magnetic resonance imaging; MUS, mercaptoundecylsulfonic acid; NMR, nuclear magnetic resonance; NP, nanoparticle; OT, octanethiol; SQUID, superconducting quantum interference device:; TEM, transmission electron microscopy; XPS, X-ray photoelectron spectroscopy; XRD, X-ray powder diffraction

■ REFERENCES

(1) Rudin, M., and Weissleder, R. (2003) Molecular imaging in drug discovery and development. *Nat. Rev. Drug Discovery 2*, 123−131.
(2) Lee, H., Shin, T.-H., Cheon, J., and Weissleder, R. (2015) Recent Developments in Magnetic Diagnostic Systems. *Chem. Rev. 115*, 10690−10724.
(3) Rogers, W. J., Meyer, C. H., and Kramer, C. M. (2006) Technology Insight: in vivo cell tracking by use of MRI. *Nat. Clin. Pract. Cardiovasc. Med. 3*, 554−562.
(4) Villaraza, A. J. L., Bumb, A., and Brechbiel, M. W. (2010) Macromolecules, dendrimers, and nanomaterials in magnetic resonance imaging: the interplay between size, function, and pharmacokinetics. *Chem. Rev. 110*, 2921−2959.
(5) Verma, A., Uzun, O., Hu, Y., Hu, Y., Han, H.-S., Watson, N., Chen, S., Irvine, D. J., and Stellacci, F. (2008) Surface-structure-regulated cell-membrane penetration by monolayer-protected nanoparticles. *Nat. Mater. 7*, 588−595.
(6) Duncan, R., and Richardson, S. C. W. (2012) Endocytosis and Intracellular Trafficking as Gateways for Nanomedicine Delivery: Opportunities and Challenges. *Mol. Pharmaceutics 9*, 2380−2402.

DOI: 10.1021/acs.bioconjchem.6b00577
Bioconjugate Chem. 2017, 28, 161−170

(7) Beddoes, C. M., Case, C. P., and Briscoe, W. H. (2015) Understanding nanoparticle cellular entry: A physicochemical perspective. *Adv. Colloid Interface Sci. 218*, 48−68.
(8) Arbab, A. S., Bashaw, L. A., Miller, B. R., Jordan, E. K., Lewis, B. K., Kalish, H., and Frank, J. A. (2003) Characterization of Biophysical and Metabolic Properties of Cells Labeled with Superparamagnetic Iron Oxide Nanoparticles and Transfection Agent for Cellular MR Imaging. *Radiology 229*, 838.
(9) Bulte, J. W. M., Douglas, T., Witwer, B., Zhang, S.-C., Strable, E., Lewis, B. K., Zywicke, H., Miller, B., van Gelderen, P., Moskowitz, B. M., et al. (2001) Magnetodendrimers allow endosomal magnetic labeling and in vivo tracking of stem cells. *Nat. Biotechnol. 19*, 1141−1147.
(10) Pan, B., Cui, D., Sheng, Y., Ozkan, C., Gao, F., He, R., Li, Q., Xu, P., and Huang, T. (2007) Dendrimer-modified magnetic nanoparticles enhance efficiency of gene delivery system. *Cancer Res. 67*, 8156−8163.
(11) Wang, L., Park, H.-Y., Lim, S. I.-I., Schadt, M. J., Mott, D., Luo, J., Wang, X., and Zhong, C.-J. (2008) Core@shell nanomaterials: gold-coated magnetic oxide nanoparticles. *J. Mater. Chem. 18*, 2629.
(12) Amendola, V., Saija, R., Maragò, O. M., and Iatì, M. A. (2015) Superior plasmon absorption in iron-doped gold nanoparticles. *Nanoscale 7*, 8782−8792.
(13) Amendola, V., Scaramuzza, S., Litti, L., Meneghetti, M., Zuccolotto, G., Rosato, A., Nicolato, E., Marzola, P., Fracasso, G., Anselmi, C., et al. (2014) Magneto-plasmonic Au-Fe alloy nanoparticles designed for multimodal SERS-MRI-CT imaging. *Small 10*, 2476−2486.
(14) Dahal, N., Chikan, V., Jasinski, J., and Leppert, V. J. (2008) Synthesis of Water-Soluble Iron−Gold Alloy Nanoparticles. *Chem. Mater. 20*, 6389−6395.
(15) Liu, H. L., Wu, J. H., Min, J. H., and Kim, Y. K. (2008) Synthesis of monosized magnetic-optical AuFe alloy nanoparticles. *J. Appl. Phys. 103*, 07D529.
(16) Liu, H., Zhang, W., Hou, P., and Wu, J. (2011) Facile growth of monocrystalline gold−iron nanocrystals by polymer nanoemulsion. *Gold Bull. 44*, 21−25.
(17) Curtis, A., Malekigorji, M., and Holman, J. (2015) Heat Dissipation of Hybrid Iron Oxide-Gold Nanoparticles in an Agar Phantom. *J. Nanomed. Nanotechnol. 06*, 335.
(18) Verma, A., and Stellacci, F. (2010) Effect of Surface Properties on Nanoparticle-Cell Interactions. *Small 6*, 12−21.
(19) Carney, R. P., Carney, T. M., Mueller, M., and Stellacci, F. (2012) Dynamic cellular uptake of mixed-monolayer protected nanoparticles. *Biointerphases 7*, 17−9.
(20) Amendola, V., Scaramuzza, S., Agnoli, S., Polizzi, S., and Meneghetti, M. (2014) Strong dependence of surface plasmon resonance and surface enhanced Raman scattering on the composition of Au-Fe nanoalloys. *Nanoscale 6*, 1423−1433.
(21) Amendola, V., Meneghetti, M., Bakr, O. M., Riello, P., Polizzi, S., Anjum, D. H., Fiameni, S., Arosio, P., Orlando, T., de Julian Fernandez, C., et al. (2013) Coexistence of plasmonic and magnetic properties in Au89Fe11 nanoalloys. *Nanoscale 5*, 5611−5619.
(22) Carril, M., Fernández, I., Rodríguez, J., García, I., and Penadés, S. (2014) Gold-Coated Iron Oxide Glyconanoparticles for MRI, CT, and US Multimodal Imaging. *Part. Part. Syst. Charact. 31*, 81−87.
(23) Chiang, I.-C., and Chen, D. H. (2007) Synthesis of Monodisperse FeAu Nanoparticles with Tunable Magnetic and Optical Properties. *Adv. Funct. Mater. 17*, 1311−1316.
(24) Chung, R. J., Wang, H. Y., and Wu, K. T. (2014) Preparation and characterization of Fe-Au alloy nanoparticles for hyperthermia application. *J. Med. Biol. Eng. 34*, 251−255.
(25) Hoskins, C., Min, Y., Gueorguieva, M., McDougall, C., Volovick, A., Prentice, P., Wang, Z., Melzer, A., Cuschieri, A., and Wang, L. (2012) Hybrid gold-iron oxide nanoparticles as a multifunctional platform for biomedical application. *J. Nanobiotechnol. 10*, 27.
(26) Velasco, V., Pohl, D., Surrey, A., Bonatto-Minella, A., Hernando, A., Crespo, P., and Rellinghaus, B. (2014) On the stability of AuFe alloy nanoparticles. *Nanotechnology 25*, 215703−215703.
(27) Gawande, M. B., Goswami, A., Asefa, T., Guo, H., Biradar, A. V., Peng, D.-L., Zboril, R., and Varma, R. S. (2015) Core-shell nanoparticles: synthesis and applications in catalysis and electrocatalysis. *Chem. Soc. Rev. 44*, 7540−7590.
(28) Ghosh Chaudhuri, R., and Paria, S. (2012) Core/Shell Nanoparticles: Classes, Properties, Synthesis Mechanisms, Characterization, and Applications. *Chem. Rev. 112*, 2373−2433.
(29) Chang, W.-S., Park, J.-W., Rawat, V., Sands, T., and Lee, G. U. (2006) Templated synthesis of gold−iron alloy nanoparticles using pulsed laser deposition. *Nanotechnology 17*, 5131−5135.
(30) Sohn, Y., Pradhan, D., Kang, J.-S., and Leung, K. T. (2015) Nanoscale architecture of bimetallic hybrid Fe−Au nanostructures with and without 1,4-phenylene diisocyanide pre-functionalization. *RSC Adv. 5*, 31472−31478.
(31) Liu, H., Hou, P., Zhang, W., Kim, Y. K., and Wu, J. (2010) The synthesis and characterization of polymer-coated FeAu multifunctional nanoparticles. *Nanotechnology 21*, 335602.
(32) de Julián Fernández, C., Mattei, G., Paz, E., Novak, R. L., Cavigli, L., Bogani, L., Palomares, F. J., Mazzoldi, P., and Caneschi, A. (2010) Coupling between magnetic and optical properties of stable Au−Fe solid solution nanoparticles. *Nanotechnology 21*, 165701.
(33) Saha, D. K., Koga, K., and Takeo, H. (1999) Stable icosahedral nanoparticles in an as-grown AuFe alloy. *Eur. Phys. J. D 9*, 539.
(34) Carroll, K. J., Hudgins, D. M., Spurgeon, S., Kemner, K. M., Mishra, B., Boyanov, M. I., Brown, L. W., III, Taheri, M. L., and Carpenter, E. E. (2010) One-Pot Aqueous Synthesis of Fe and Ag Core/Shell Nanoparticles. *Chem. Mater. 22*, 6291−6296.
(35) Chaubey, G. S., Barcena, C., Poudyal, N., Rong, C., Gao, J., Sun, S., and Liu, J. P. (2007) Synthesis and Stabilization of FeCo Nanoparticles. *J. Am. Chem. Soc. 129*, 7214.
(36) Jackson, A. M., Myerson, J. W., and Stellacci, F. (2004) Spontaneous assembly of subnanometre-ordered domains in the ligand shell of monolayer-protected nanoparticles. *Nat. Mater. 3*, 330−336.
(37) Alkilany, A. M., Nagaria, P. K., Hexel, C. R., Shaw, T. J., Murphy, C. J., and Wyatt, M. D. (2009) Cellular Uptake and Cytotoxicity of Gold Nanorods: Molecular Origin of Cytotoxicity and Surface Effects. *Small 5*, 701−708.
(38) Ferrando, R., Jellinek, J., and Johnston, R. L. (2008) Nanoalloys: From Theory to Applications of Alloy Clusters and Nanoparticles. *Chem. Rev. 108*, 845−910.
(39) Bogani, L., Cavigli, L., de Julian Fernandez, C., Mazzoldi, P., Mattei, G., Gurioli, M., Dressel, M., and Gatteschi, D. (2010) Photocoercivity of nano-stabilized Au: Fe superparamagnetic nanoparticles. *Adv. Mater. 22*, 4054−4058.
(40) Liu, W., Qian, T.-T., and Jiang, H. (2014) Bimetallic Fe nanoparticles: Recent advances in synthesis and application in catalytic elimination of environmental pollutants. *Chem. Eng. J. 236*, 448−463.
(41) Okamoto, H., Massalski, T. B., Swartzendruber, L. J., and Beck, P. A. (1984) The Au-Fe (Gold-Iron) system. *Bull. Alloy Phase Diagrams 5*, 592−601.
(42) Cannella, V., and Mydosh, J. A. (1972) Magnetic ordering in gold-iron alloys. *Phys. Rev. B 6*, 4220−4237.
(43) Chepulskii, R. V., Butler, W. H., van de Walle, A., and Curtarolo, S. (2010) Surface segregation in nanoparticles from first principles: The case of FePt. *Scr. Mater. 62*, 179.
(44) Ghosh, A., Basak, S., Wunsch, B. H., Kumar, R., and Stellacci, F. (2011) Effect of composition on the catalytic properties of mixed-ligand-coated gold nanoparticles. *Angew. Chem., Int. Ed. 50*, 7900−7905.
(45) Bondi, J. F., Misra, R., Ke, X., Sines, I. T., Schiffer, P., and Schaak, R. E. (2010) Optimized Synthesis and Magnetic Properties of Intermetallic Au 3 Fe 1− x, Au 3 Co 1− x, and Au 3 Ni 1− x Nanoparticles. *Chem. Mater. 22*, 3988.
(46) Vasquez, Y., Luo, Z., and Schaak, R. E. (2008) Low-temperature solution synthesis of the non-equilibrium ordered intermetallic compounds Au3Fe, Au3Co, and Au3Ni as nanocrystals. *J. Am. Chem. Soc. 130*, 11866−11867.

DOI: 10.1021/acs.bioconjchem.6b00577
Bioconjugate Chem. 2017, 28, 161−170

(47) Lee, N., and Hyeon, T. (2012) Designed synthesis of uniformly sized iron oxide nanoparticles for efficient magnetic resonance imaging contrast agents. *Chem. Soc. Rev. 41*, 2575−2589.
(48) Kuna, J. J., Voïtchovsky, K., Singh, C., Jiang, H., Mwenifumbo, S., Ghorai, P. K., Stevens, M. M., Glotzer, S. C., and Stellacci, F. (2009) The effect of nanometre-scale structure on interfacial energy. *Nat. Mater. 8*, 837−842.
(49) Georgiadis, J. G., and Ramaswamy, M. (2005) Magnetic resonance imaging of water freezing in packed beds cooled from below. *Int. J. Heat Mass Transfer 48*, 1064.
(50) Donahue, K. M., Weisskoff, R. M., and Burstein, D. (1997) Water diffusion and exchange as they influence contrast enhancement. *Journal of Magnetic Resonance Imaging 7*, 102−110.
(51) Andreozzi, P., Martinelli, C., Carney, R. P., Carney, T. M., and Stellacci, F. (2013) Erythrocyte incubation as a method for free-dye presence determination in fluorescently labeled nanoparticles. *Mol. Pharmaceutics 10*, 875−882.
(52) Sabella, S., Carney, R. P., Brunetti, V., Malvindi, M. A., Al-Juffali, N., Vecchio, G., Janes, S. M., Bakr, O. M., Cingolani, R., Stellacci, F., et al. (2014) A general mechanism for intracellular toxicity of metal-containing nanoparticles. *Nanoscale 6*, 7052−7061.
(53) Sosnovik, D. E., and Weissleder, R. (2007) Emerging concepts in molecular MRI. *Curr. Opin. Biotechnol. 18*, 4−10.
(54) Carney, R. P., Astier, Y., Carney, T. M., Voïtchovsky, K., Jacob Silva, P. H., and Stellacci, F. (2013) Electrical method to quantify nanoparticle interaction with lipid bilayers. *ACS Nano 7*, 932−942.
(55) Lewis, D. J., Day, T. M., MacPherson, J. V., and Pikramenou, Z. (2006) Luminescent nanobeads: attachment of surface reactive Eu(iii) complexes to gold nanoparticles. *Chem. Commun.*, 1433.

DOI: 10.1021/acs.bioconjchem.6b00577
Bioconjugate Chem. 2017, 28, 161−170